Research Article Vol. 15, No. 8 / 1 Aug 2025 / Optical Materials Express 1913
Optical Materials EXPRESS

Ultra-thin photonic crystal slab metalenses [Invited]

YUDONG CHEN, MINGSEN PAN, YUZE SUN, AND WEIDONG ZHOU*

Department of Electrical Engineering, Photonics Center, University of Texas at Arlington, Arlington, TX 76019, USA
*wzhou@uta.edu

Abstract: We report a novel ultra-thin metalens design based on photonic crystal slab (PCS) resonance modes. We experimentally verified with a metalens structure based on amorphous silicon on a quartz material platform by implementing the optical guided resonance on the PCS. The PCS metalens designs feature an ultra-thin device layer of about 160 nm at an operation wavelength of 940 nm. A full 2π transmission phase transition is realized by varying the air hole sizes at the design wavelength. Metalens devices with different phase change gradients were designed and fabricated to achieve different NAs. A maximum of 86.4% focusing efficiency is achieved. Imaging capabilities are characterized, and clear images are observed within the field of view. The PC resonance-based phase modulation design can be applied to optical beam manipulation, phase plate design, imaging, and laser beam formation applications.

1. Introduction

Optical metalenses, or flat lenses, offer advantages over traditional lenses by manipulating light using subwavelength structures, enabling compact, efficient, and multifunctional optical systems [1–5]. They are lighter, thinner, and more compact, potentially replacing conventional optical components in integrated or microscale optics. Dielectric transparent materials are typically used to achieve low loss high focusing efficiency (EF). However, to ensure sufficient index contrast, typically higher index metasurface structure materials are needed on a relatively low index transparent substrate. This results in certain material challenges when designing metalens for different spectral band operations, as shown in Fig. 1. In the ultraviolet range, Zhang *et al*. reported a 71.8% EF HfO_2 metalens at 325 nm, with 550 nm nano-pillar height [6]. At visible wavelength, the highest EF metalens reported is a GaN metalens with 600 nm height nano-pillars, with an EF 91.6% at 532 nm [7]. The TiO_2 metalens has an EF of 96% at 405 nm wavelength with 600 nm height nano-fins structure [8]. At near-infrared range, a-Si or Si material are commonly used in order to be CMOS process compatible. An EF of 42.7% was reported at 1550 nm with 5 µm tall Si pillar-based metalens [9]. Amorphous-Si (a-Si) metalens [10] experimentally demonstrated an EF 70% at 850 nm wavelength with 480 nm height nano-pillar. In the mid-infrared range, GaSb was used to confine light. The structure is a nano-pillar structure with 2 µm height, which can achieve 52% EF at 3.3µm wavelength [11]. Based on $Ge_2Sb_2Se_4Te_1$(GSST) non-volatile optical phase-change material, a reconfigurable metalens at 5.2 mm wavelength was reported with 1 mm height pillars [4]. Si material is also a good material for the mid- and long-wave infrared ranges. An a-Si nano-pillar metalens of 2 µm height, which could achieve 78% EF at 4 µm wavelength [12]. Hung *et al.* reported a c-Si nano-pillar metalens operating at 10.6 mm, with a pillar height of 12 mm and 51% EF [13].

So far, optical metalenses are designed based on well-established design principles in optical metamaterials or metasurfaces. Individual dielectric elements (mostly isolated pillars) or meta-atoms are carefully designed for the desired phase tuning ranges (Fig. 1). As explained later, these dielectric pillars often have high aspect ratios, where a certain height is needed to achieve full 2π

#564211 https://doi.org/10.1364/OME.564211
Journal © 2025 Received 6 Apr 2025; revised 1 Jul 2025; accepted 2 Jul 2025; published 15 Jul 2025

Optical Materials EXPRESS

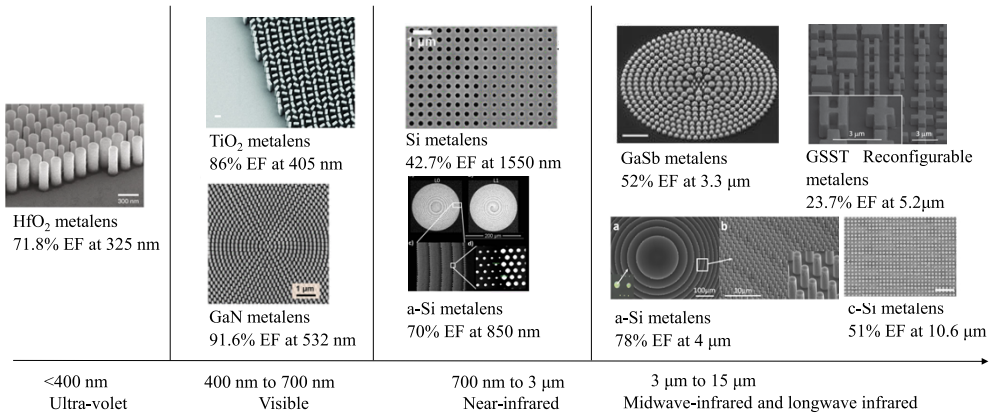

Fig. 1. Achromatic metalenses with different materials for different operation spectral bands: (a) HfO_2 nano-pillar metalens [6] operating in UV range; (b) TiO_2 and GaN nano-fins metalens [7,8] operating in visible range; (c) Deep etched holy Si metalens and a-Si nano-pillar metalens [9,10] operating in near-infrared range; (d) GaSb, GSST, a-Si, and c-Si nano-pillar metalens [11,12] [4] [13] operating in the midwave and longwave-infrared ranges.

phase control capabilities. Such isolated pillar array metalens structures are harder to fabricate, which results in certain reliability challenges. Thus, attempts have been made to achieve holy metalenses or inverted meta-atoms. The first application of a complementary Babine-inverted resonator structure was reported by Falcone *et al.* [14] For the dielectric system, Park *et al.* reported effective index modulation with silicon through-holes for terahertz focusing [15]. Wang *et al.* working for pillar and holes achromatic metalens based on GaN platform [16]. Lim *et al.* reported a high aspect ratio holey metalens [9]. However, these holy metalenses typically have high aspect ratio as well, as the design principles are the same as the isolated dielectric pillar structures.

Here, we report ultra-thin metalens based on air hole photonic crystal slabs (PCS) with high EF. In what follows, we will first describe the design principles of metalens and the approaches to achieve high EF PCS Metalens based on the strong resonances in these PCS structures to achieve full 2π phase tuning with ultra-thin slabs. We will then report the experimental demonstration of these ultra-thin (160 nm) PCS metalens operating at 940 nm wavelength with different focusing capabilities and high EF (86%). These PCS metalenses have a much thinner thickness and thus much better mechanical robustness than the metasurface metalenses (often with high aspect ratio pillar structures). [9,17–19]

2. Metalens design principles

Most of the conventional metalens design tried to pursue the high aspect ratio because they are working for broadband, and high aspect ratio is easy to achieve the 2π phase control. In that case, the transmission phase could be described as:$\varphi = \frac{2\pi}{\lambda}(n_{eff} - 1)h$, where λ is the incident light wavelength, h is the height of the nanofin and n_{eff} is effective index of refraction related to different structure sizes [9]. The group delay represented by phase derivative with angular frequency can be described below:

$$\frac{\partial \varphi}{\partial \omega} = \frac{1}{c}(n_{eff} - 1)h + \frac{\omega}{c}\frac{\partial n_{eff}}{\partial \omega}h \tag{1}$$

The conventional metalens design considers the broadband working wavelength (>100 nm), thus, the first term in the Eq. (1) should be the dominant part. The second term is represented by

Optical Materials EXPRESS

the structure details to fine tuning the phase change details. For achieving the 2π phase changing, the thickness of the nanopillar has a limitation of $h > \frac{\lambda}{(n_{eff}-1)}$. This often leads to very high height (h values) for the resulting metalens [1].

On the other hand, much thinner metalens can be achieved if we consider designs where strong dispersion is considered, i.e. large dominant second term in Eq. (1). We consider 2D air hole PCS structures where the dispersion engineering can lead to much thinner metalenses. We consider here mostly narrow spectral band operations, though broadband is feasible with careful designs and mixed lattice designs. There are many applications, where narrow spectral bands are sufficient, such as laser-based communications, infrared imaging, and sensing systems.

For a typical metalens design, there are three major steps: (1) Construct 2π phase change of different uniform PCS structures; (2) Design a target phase map with metalens; (3) Match the target metalens phase with the 2π phase change PCS structure. The metalens design process starts with the study of the uniform PCS unit cell phase control. As reported earlier [20], we simplify the mode to scattering matrix of asymmetric two-port system that can be derived as [21]

$$\boldsymbol{S}(\omega, r, a) = \boldsymbol{C}(\omega, r, a) + \frac{dd^T}{j(\omega - \omega_0) + \frac{1}{\tau}} \tag{2}$$

The first term is the background scattering matrix $C = exp(j\theta)\begin{bmatrix} r & jt \\ jt & r \end{bmatrix}$, where r, t and θ are real constant with $r^2 + t^2 = 1$, $d = [d_1 d_2]^T$ is the coupling constant and $\tau = 2Q(r,a)/\omega$ is photon life time and the transmittance [22] is $\boldsymbol{t} = |t|\exp\left[j\frac{2\pi}{\lambda}(n_{eff}-1)h\right]$. Where n_{eff} is the effective index without considering resonance. By using temporal coupled-mode theory [20,23], the transmission coefficient of a two-port system can be derived as

$$S_{21}(\omega, r, a) = C_{21}(\omega, r, a) + d(\omega, r, a)d_2^* d_1 \tag{3}$$

where $d(\omega, r, a) = \frac{1}{j(\omega-\omega_0)+1/\tau(r,a)}$ is the line shape function of resonance mode which correlated with the optical phase to change the effective thickness. Figure 2(a) shows uniform asymmetric (Si on SiO_2) PCS two-port scattering mode. Figure 2(b) shows the schematic of the scattering matrix phase profile on the complex plane. It can be seen that one sufficient condition to achieve 2π transmission phase controlling is

$$|d_2^* d_1| > |t|/|d(\omega, r, a)| \tag{4}$$

On the other hand, the transmission coefficient of waves going through the PCS structure can be described as [22,24,25]

$$S_{21}(\omega, r, a) = |t|\exp\left[j\frac{2\pi}{\lambda}(n_g - 1)h\right] \tag{5}$$

where n_g is group index which could be larger than the material index due to the group velocity delayed by PCS resonance. And group index can be described as

$$n_g = n_{eff} + \omega\frac{\partial n_{eff}}{\partial \omega} \tag{6}$$

where $\omega = 2\pi f$ is angular frequency of the resonance spectrum. The transmission phase difference is [22,25]

$$\varphi = \frac{2\pi}{\lambda}(n_g - 1)h \tag{7}$$

where h is the thickness of the PCS layer.

Optical Materials EXPRESS

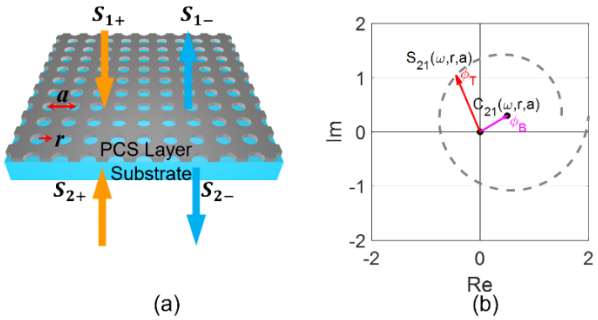

Fig. 2. A two-port system modelling for coupled mode analysis of PCS transmission phase. (a) Schematic of the asymmetric (e.g. Si on SiO_2) PCS two-port scattering model. (b) Schematic of the scattering matrix profile on the complex plane. $\emptyset_B$ is the background transmission phase shift and $\emptyset_T$ is the total transmission phase with PCS. To achieve the completely 2π phase shifting, the sufficient condition is S21 (ω, r, a) curve encircles the zero point within a spectral range.

The first term (n_{eff}) from Eq. (6) is the dominant term to control the phase. For metalenses working in a broadband spectral range (e.g., > 100 nm) [9,18,26,27], the device has a minimum thickness limitation to achieve the 2π phase shift. For example, the lens thickness for a 940 nm metalens should be at least thicker than $h > \frac{\lambda}{n_g - 1} \sim \frac{\lambda}{n_{eff} - 1} = 350\ nm$, assuming $n_{eff} = 3.68$ limited by the material index [28]. In this paper, we used the PCS structure to enhance the group delay, which makes the second term become a dominant part that can result in higher group index than the material index itself. This removes the thickness limitation to achieve 2π phase control. To study the phase and index relation, we investigate a PCS structure based on a-Si/SiO_2 material system at operation wavelength of 940 nm, as shown in Fig. 2(a). The simulation is carried out with rigorous coupled-wave analysis (RCWA) S4 software [29].

The PCS layer contains uniform circular air holes within a square lattice (lattice constant: a, radius: r, device thickness: h).

Figure 3(a) shows the parameter sweeping of h from 0.1 to 5 μm and r/a from 0.3 to 0.45. When the PC thickness increases, the range to achieve the 2π phase increases, because when the PC thickness increases, the first term (n_{eff}) of Eq. (6) will dominate the group index change. It is worth noting that a thickness of PCS layer as thin as h = 160 nm can support 2π phase shift, as shown in Fig. 3(b), due to the guided resonances in the PCS.

Figure 3(c) and (d) show the 1D plots of 2π phase shift for h = 160 nm and 300 nm respectively. So, the second term ($\omega \frac{\partial n_{eff}}{\partial \omega}$) of Eq. (6) becomes the dominant part of the n_g. These are much thinner than the thickness of 350 nm required to achieve 2π phase change, if we only consider the first term in Eq. (1). For slab thickness of 350 nm, abrupt change of phase may happen as shown in Fig. 3(d) due to the multimode coupling when high-order modes are allowed in the thicker slab.

Based on the design principle outlined above, we simulate the transmittance and transmission phase of uniform PCS structure. Figure 4(a) and (b) show the transmission phase and transmittance change with varying lattice constant (a) and air filling ratio (r/a). respectively. The design target is to find the maximal transmission and a full 2π phase change by varying the air hole radius. An optimal PCS thickness of h = 160 nm and lattice constant of a = 500 nm are retrieved for 940 nm wavelength. With variation of the air hole diameter between 150 nm to 480 nm (0.15 < r/a < 0.48), as shown in Fig. 4(c), a full 2π phase shift can be achieved. Further, when the diameter is between 300 nm to 450 nm (0.3 < r/a < 0.45), the 2π phase could be controlled with transmission higher than 82%, as shown in Fig. 4(d).

Optical Materials EXPRESS

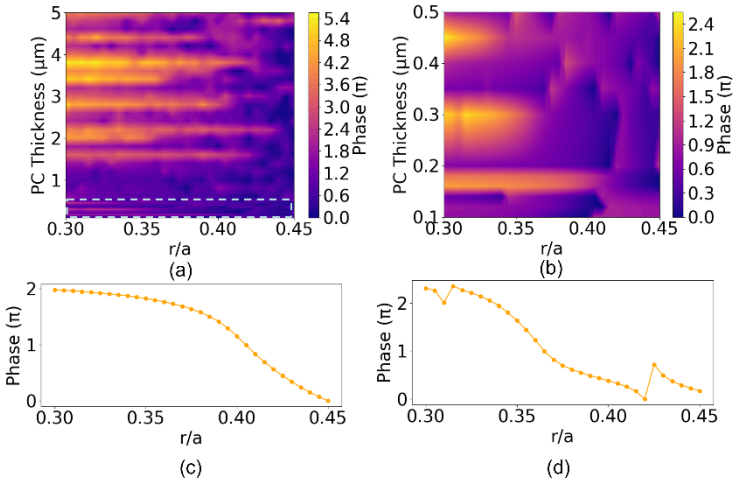

Fig. 3. PCS transmission phase change relations at 940 nm. (a) The transmission phase changes with radius over lattice ratio (r/a) and different PC layer thicknesses (h), the white dash box is the zoom region; (b) Zoom-in of (a) with h = 0.1 μm to 0.5 μm; (c) The 1D plot for the phase changing of different r/a with h = 160 nm; (d) The 1D plot for the phase changing of different r/a with h = 300 nm.

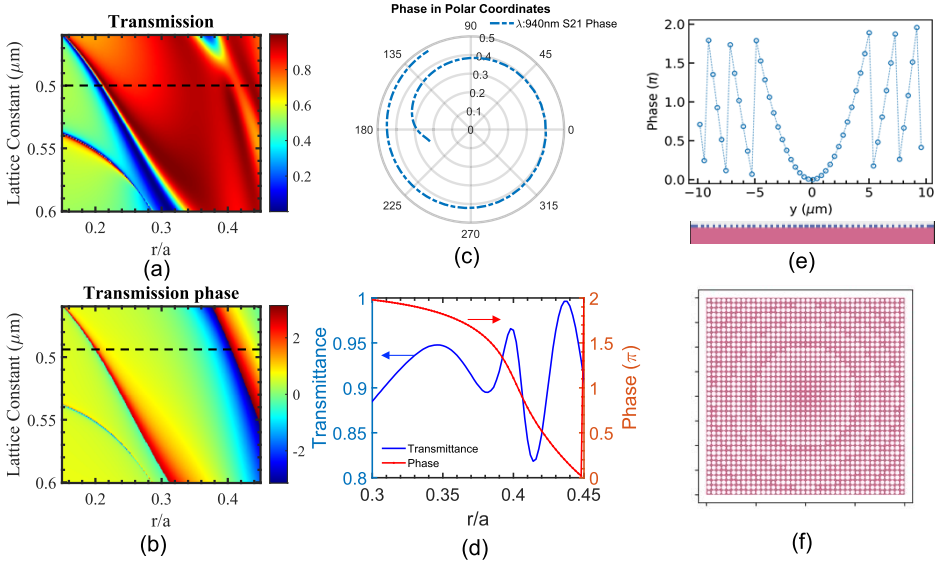

Fig. 4. Design and simulation of PCS-based metalens. Simulated transmission (a) phase and (b) amplitude (z-axis) contours for different r/a ratio (x-axis) and different lattice constant (y-axis); (c) Transmission phase on polar coordinates with different r/a ratio at lattice constant of 500 nm (cross cutting of black dash line within transmission and phase map); (d) The transmittance (left y-axis) and phase change in transmission (right y-axis) for different r/a with lattice constant of 500 nm; (e) Metalens (NA = 0.6) phase design by varying the air hole size along the x-axis at y = 0. The bottom blue square is the cross section of the a-Si PCS pattern, and the pink area is SiO_2. And (f) Schematic of nanostructure distribution matching with the metalens ($20\mu m \times 20\mu m$) phase distribution for NA = 0.6.

Optical Materials EXPRESS

The second step is calculating the metalens target phase profile $\varphi(x, y)$ at the design wavelength (940 nm for this work). To make the phase profile function like a spherical lens, which focuses a normally incident plane wave to diffraction limitation, the phase profile needs to follow [30]

$$\varphi(x, y, \omega) = -\frac{\omega}{c}\left(\sqrt{x^2 + x^2 + f^2} - f\right) \tag{8}$$

where ω is angular frequency of light, c is free-space speed of light, $f = \frac{D}{2NA}\sqrt{1 - NA^2}$ is focal length, D is lens diameter, and NA is numerical aperture. The optimized phase profile along the x-axis is the warped hyperbolic one, as shown in Fig. 4(e), with the cross section of the nano PCS structures shown as blue blocks below that. In our previous report [31], we validated the metalens design function with Tidy3D [31,32]. The simulation mode considers the metalens of 20 $\mu m \times 20$ μm area at 940 nm of NA = 0.6, and Fig. 4(f) shows the correlation between nanostructure size and 2D metalens phase profile.

3. PCS metalens performance

PCS metalens fabrication starts with the deposition of a 158 nm layer of a-Si on a quartz wafer. PCS patterning was carried out based on the standard electron-beam lithography (EBL) and reactive ion etching (RIE) processes. Multiple 500 mm-sized PCS metalenses were fabricated with different NAs. Another 1 mm-sized PCS metalens was also fabricated with NA = 0.15. Figure 5(a) to (d) show the scanning electron microscopy (SEM) images of PCS metalenses at different length scales. The air hole size change is smooth and matches the phase map design of Eq. (8). It is also worth noting that due to the symmetry of circular air holes and square lattice design, the PCS metalens reported here is polarization insensitive.

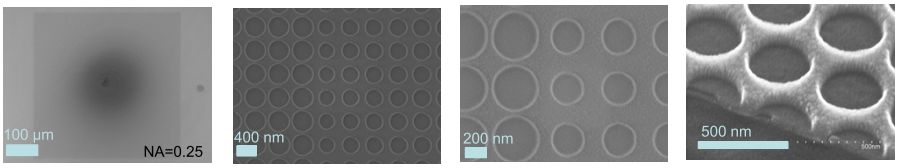

Fig. 5. SEM images of a PCS metalens. (a)Top view of one entire device for NA = 0.25, and device size 500 µm. (b)-(c) zoom-in images of (a). (d) Cross-sectional view.

Figure 6(a) shows the focus ability measurement setup, which contains a white light laser source (with bandpass filters centered at 780 nm, 850 nm and 940 nm, respectively) and two lens 4f system (used for reducing beam size to match the metalens size), metalens device, objective lens, tube lens and beam profiling camera. The objective lens, combined with the tube lens, is used to amplify the focal beam spot. In the measurement setup, the image captured by the camera is 10 times magnification of real target demension. We also use the stage to move the image system along the optical axis of the metalens and track the beam-focusing performances. Figure 6(b) shows the imaging ability measurement setup, which is similar to the focusing ability measurement setup. A diffuser is used to reduce laser coherence to avoid the speckle effect.

To study metalens devices, we first investigate the performance of the focal length. Shown in Fig. 7(a) to (e) are the measured field distributions for different NAs. Based on these results, the focal lengths and the focus beam spot sizes can be derived. Figure 8 shows that the measured and designed focal lengths agree well for different NA values. Figure 8(b) shows the average beam size changing of different wavelengths follow the same tendency with 940 nm incident light, the beam size reduces with increasing NA. The experimental results follow the theoretical estimation tendency with a small offset.

Optical Materials EXPRESS

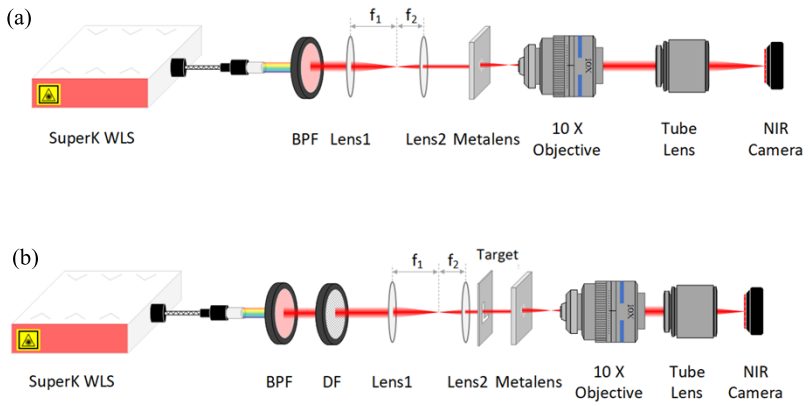

Fig. 6. Schematics of the testing setup for the metalens (a) beam spot and working distance measurement setup, and (b) imaging measurement setup.

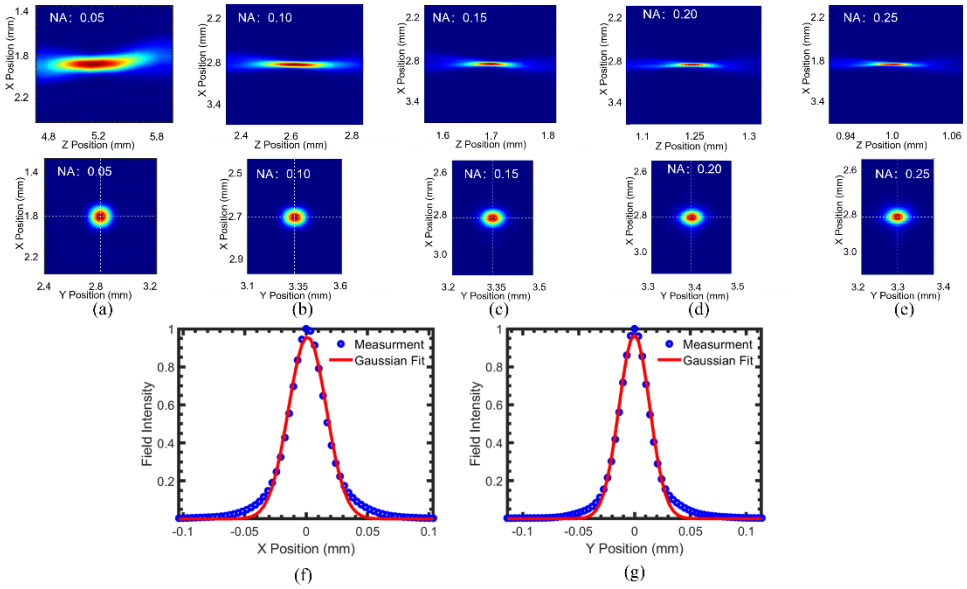

Fig. 7. Measured field intensity of a 940 nm collimated light beam. (a-e) Field distribution of light beam passing through metalens on the x-z propagation plane (top row, for focal lengths measurement) and along x-y focal plane (bottom row, for spot size measurement). (f, g) 1D field intensity plots along x and y directions at focus plane for NA = 0.25 metalens.

The focusing efficiency (EF) is characterized for evaluating the metalens imaging ability. The EF is defined as the ratio of the light intensity (energy) within the 3 times of focusing beam FWHM area to the total intensity (energy) at the focal plane [33]. EF can be extracted based on the 1D field distribution plots at the focal plane, as shown in Fig. 7(f, g). Gaussian fits were used to fit into the field distribution profiles. The highest focusing efficiency is 86.4% at 940 nm with NA = 0.25. Figure 9 shows focal efficiency with different wavelengths (905 to 980 nm) for PCS metalens with different NAs. EF remains higher than 80% from 940 to 950 nm and gradually reduces to 20% at 930 nm and 960 nm. In this case, we can consider our device's

Optical Materials EXPRESS

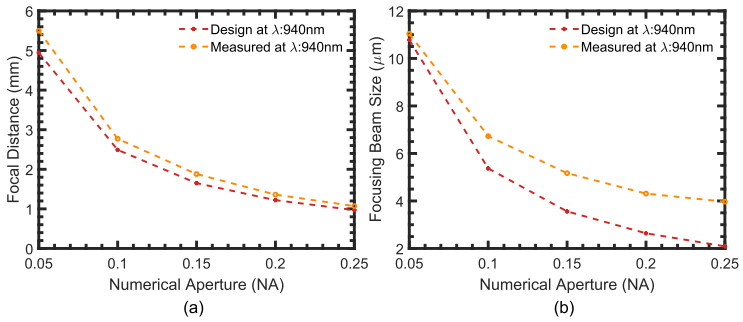

Fig. 8. Measurement results for metalens performances. (a) Measured and designed focal lengths of metalenses with different numerical apertures (NAs). (b) The focal spot beam size for metalenses with different NAs.

working bandwidth to be 940 nm to 950 nm. For smaller NAs, the EFs reduce to 44% at 940 nm for NA of 0.05. It is still a relatively high EF for the imaging ability test.

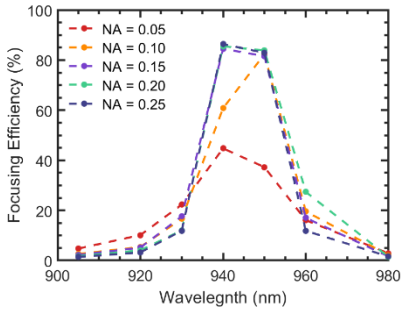

Fig. 9. Measured focusing efficiency (EF) from 900 nm to 980 nm wavelengths for PCS metalenses with different NAs. The lower EF for NA = 0.05 and 0.10 devices is mainly due to the fabrication imperfectness.

As shown in Fig. *9*, all metalens devices have very high EF near 940 nm. Unintentional defects of PCS patterning for the NA = 0.05 and NA = 0.10 devices caused lower efficiency because of the light leakage to the region outside of the focusing spot. On the focusing plan, the incident light with wavelength of 940 nm has the most suppressed background. When the incident light wavelength moves far away from 940 nm, the focusing spot of the laser beam will become more and more indistinguishable from the background. Although the working spectral range for the metalens is narrow, we have demonstrated the ultrathin PCS-based metalens structures by engineering resonance phase of the guided modes.

Figure *10* shows imaging capabilities with metalens devices designed with various NA at 940 nm. A self-made letter target sample ("UTA") is used for the imaging test, as shown in the scanning electron microscopy (SEM) image in Fig. *10*(a). Figure *10*(b) shows an image without metalens, and Fig. *10*(c) shows an image of the target with NA = 0.15 and lens size D = 1 mm for the letters with font size of 20 mm. Figure *10*(d) shows images with the same lens (D = 1 mm, NA = 0.15) on font size 40μm. Compared with Fig. *10*(c) results, the new imaging has much better resolution, with smaller field of view (FOV) capturing one letter each snapshot. So, we move the lens location to track the three different locations and show them from top to bottom in Fig. *10*(d). Similarly, Fig. *10*(e) shows the images by using metalens of D = 500 μm and NA = 0.25 for font size 20 mm. Obviously, the image of NA = 0.25 at 940 nm has the highest contrast.

Optical Materials EXPRESS

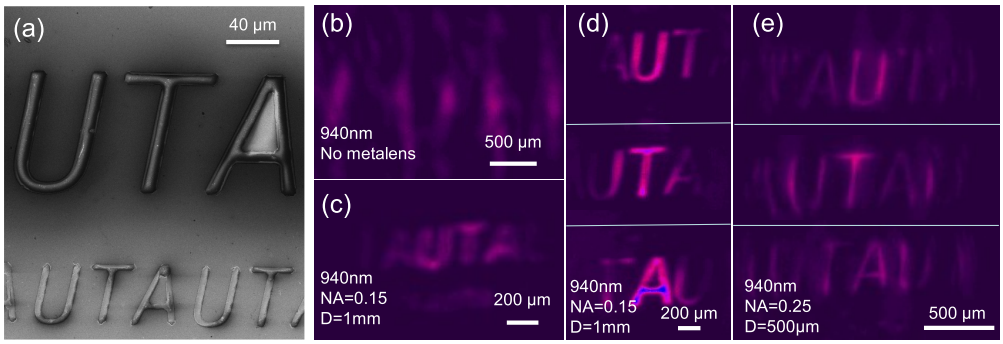

Fig. 10. PCS metalens imaging results with 940 nm wavelength light: (a) SEM of the "UTA" letters as the imaging target. Font sizes of larger and smaller texts are 40 mm and 20 mm, respectively; (b) An image without metalens; (c, d) Imaging with metalens with metalens design NA = 0.15 and device size D = 1 mm. The text size is 20 mm for (b) and 40 mm for (c); and (e) Images after PCS metalens with NA = 0.25 and device area side length D = 500 mm. Letter font size is 20 mm.

4. Conclusions

In summary, we propose and demonstrate ultra-thin air hole PCS metalenses. By implementing the optical guided resonance on the PCS, we show that ultra-thin metalens are feasible as compared to commonly reported meta-atom-based dielectric pillar metalens, as summarized in Table 1. We experimentally verified this with a metalens structure based on amorphous silicon on a quartz material platform. The PCS metalens designs feature an ultra-thin device layer of about 160 nm at an operation wavelength of 940 nm. Full 2π transmission phase transition is realized by varying the air hole sizes at the design wavelength. Metalens devices with different phase change gradients were designed and fabricated to achieve different NA. A maximum 86.4%

Table 1. Summary of performance metrics for achromatic metalenses

Wavelength (μm)	Device thickness (nm)	Material	EF (%)[a]	Diameter (μm)	NA	Polarization	Ref.
0.94-0.95	160	a-Si	86.4 (M)	500	0.25	Insensitive	This work
0.43-0.63	600	GaN	91.6 (M)	100	0.164	Circular	[17]
0.4-0.7	600	TiO_2	86 (M)	240	0.8	Circular	[8]
0.65-1	1,500	TiO_2	89 (M)	25	0.1	Insensitive	[34]
~0.85	480	a-Si	70 (M)	200	0.7	Insensitive	[10]
1-1.2	1,000	Si	45 (S)	38	03	Circular	[35]
1.3-1.66	800	a-Si	55 (M)	100	0.24	Insensitive	[36]
1.47-1.59	800	Si	27 (S)	64	0.81	Circular	[37]
1.4-1.74	5,000	Si	42.7 (M)	2,000	0.24	Insensitive	[9]
3-4	2,000	GaSb	52 (M)	30	0.35	Insensitive	[11]
3.7-4.2	2,000	a-Si	78 (M)	300	0.45	Insensitive	[12]
3.7-4.5	4,000	Si	20 (S)	77	0.8	Circular	[38]
5.2	1,000	GSST	23.7 (M)			Insensitive	[4]
10.6	12,000	c-Si	51 (M)			Insensitive	[13]

[a]M: Measured; S: Simulated

Optical Materials EXPRESS

focusing efficiency is achieved. Imaging capabilities are characterized, and clear images are observed within the field of view. The PC resonance-based phase modulation design can be applied to optical beam manipulation, phase plate design, high-speed reconfigurable metalens, imaging, and laser beam formation applications.

Funding. National Science Foundation (2154109, 2213975); U.S. Department of Energy (DE-NA0004114).

Acknowledgement. Y. C. acknowledges the help from Dr. Cheng Guo on the experimental setup and the insightful discussions.

Disclosures. The authors declare that they have no known competing financial interests or personal relationships that could have appeared to influence the work reported in this paper.

Data availability. Data underlying the results presented in this paper are not publicly available at this time but may be obtained from the authors upon reasonable request.

References

1. M. Khorasaninejad and F. Capasso, "Metalenses: Versatile multifunctional photonic components," Science **358**(6367), eaam8100 (2017).
2. A. Arbabi and A. Faraon, "Advances in optical metalenses," Nat. Photonics **17**(1), 16–25 (2023).
3. M. Pan, Y. Fu, M. Zheng, *et al.*, "Dielectric metalens for miniaturized imaging systems: progress and challenges," Light: Sci. Appl. **11**(1), 195 (2022).
4. M. Y. Shalaginov, S. An, Y. Zhang, *et al.*, "Reconfigurable all-dielectric metalens with diffraction-limited performance," Nat. Commun. **12**(1), 1225 (2021).
5. F. Yang, M. Y. Shalaginov, H.-I. Lin, *et al.*, "Wide field-of-view metalens: a tutorial," Adv. Photonics **5**(03), 033001 (2023).
6. C. Zhang, S. Divitt, Q. Fan, *et al.*, "Low-loss metasurface optics down to the deep ultraviolet region," Light: Sci. Appl. **9**(1), 55 (2020).
7. B. H. Chen, P. C. Wu, V.-C. Su, *et al.*, "GaN metalens for pixel-level full-color routing at visible light," Nano Lett. **17**(10), 6345–6352 (2017).
8. M. Khorasaninejad, W. T. Chen, R. C. Devlin, *et al.*, "Metalenses at visible wavelengths: Diffraction-limited focusing and subwavelength resolution imaging," Science **352**(6290), 1190–1194 (2016).
9. S. W. D. Lim, M. L. Meretska, and F. Capasso, "A high aspect ratio inverse-designed holey metalens," Nano Lett. **21**(20), 8642–8649 (2021).
10. S. Vo, D. Fattal, W. V. Sorin, *et al.*, "Sub-wavelength grating lenses with a twist," IEEE Photonics Technol. Lett. **26**(13), 1375–1378 (2014).
11. S. Zhang, A. Soibel, S. A. Keo, *et al.*, "Solid-immersion metalenses for infrared focal plane arrays," Appl. Phys. Lett. **113**(11), 111104 (2018).
12. H. Zuo, D.-Y. Choi, X. Gai, *et al.*, "High-efficiency all-dielectric metalenses for mid-infrared imaging," Adv. Opt. Mater. **5**(23), 1700585 (2017).
13. I. L. Hung, J. Geldmeier, E. Baleine, *et al.*, "Wide field-of-view long-wave infrared metalenses," in *Proc.SPIE*, 2023, vol. 12530, p. 125300I
14. F. Falcone, T. Lopetegi, M. A. G. Laso, *et al.*, "Babinet principle applied to the design of metasurfaces and metamaterials," Phys. Rev. Lett. **93**(19), 197401 (2004).
15. S.-G. Park, K. Lee, D. Han, *et al.*, "Subwavelength silicon through-hole arrays as an all-dielectric broadband terahertz gradient index metamaterial," Appl. Phys. Lett. **105**(9), 091101 (2014).
16. S. Wang, P. C. Wu, V.-C. Su, *et al.*, "A broadband achromatic metalens in the visible," Nat. Nanotechnol. **13**(3), 227–232 (2018).
17. Y. Yang, W. Wang, P. Moitra, *et al.*, "Dielectric meta-reflectarray for broadband linear polarization conversion and optical vortex generation," Nano Lett. **14**(3), 1394–1399 (2014).
18. R. C. Devlin, M. Khorasaninejad, W. T. Chen, *et al.*, "Broadband high-efficiency dielectric metasurfaces for the visible spectrum," Proc. Natl. Acad. Sci. **113**(38), 10473–10478 (2016).
19. E. Schonbrun, K. Seo, and K. B. Crozier, "Reconfigurable imaging systems using elliptical nanowires," Nano Lett. **11**(10), 4299–4303 (2011).
20. M. Pan, Z. Liu, A. R. K. Kalapala, *et al.*, "Complete 2π phase control by photonic crystal slabs," Opt. Express **29**(25), 40795–40803 (2021).
21. S. Fan, W. Suh, and J. D. Joannopoulos, "Temporal coupled-mode theory for the Fano resonance in optical resonators," J. Opt. Soc. Am. A **20**(3), 569–572 (2003).
22. N. Yu and F. Capasso, "Flat optics with designer metasurfaces," Nat. Mater. **13**(2), 139–150 (2014).
23. S. Fan and J. Joannopoulos, "Analysis of guided resonances in photonic crystal slabs," Phys. Rev. B **65**(23), 235112 (2002).
24. T. Baba, "Slow light in photonic crystals," Nat. Photonics **2**(8), 465–473 (2008).
25. A. Figotin and I. Vitebskiy, "Slow light in photonic crystals," Waves in Random and Complex Media **16**(3), 293–382 (2006).

Optical Materials EXPRESS

26. W. T. Chen, K.-Y. Yang, C.-M. Wang, *et al.*, "High-efficiency broadband meta-hologram with polarization-controlled dual images," Nano Lett. **14**(1), 225–230 (2014).
27. W. T. Chen, A. Y. Zhu, and F. Capasso, "Flat optics with dispersion-engineered metasurfaces," Nat. Rev. Mater. **5**(8), 604–620 (2020).
28. M. S. Amin, N. Hozhabri, and R. Magnusson, "Effects of solid phase crystallization by rapid thermal annealing on the optical constants of sputtered amorphous silicon films," Thin solid films **545**, 480–484 (2013).
29. V. Liu and S. Fan, "S4: A free electromagnetic solver for layered periodic structures," Comput. Phys. Commun. **183**(10), 2233–2244 (2012).
30. F. Aieta, P. Genevet, M. A. Kats, *et al.*, "Aberration-free ultrathin flat lenses and axicons at telecom wavelengths based on plasmonic metasurfaces," Nano Lett. **12**(9), 4932–4936 (2012).
31. Z. Liu, M. Pan, A. Liu, *et al.*, "Photonic Crystal Slab Metalens," in *2022 IEEE Photonics Conference (IPC)*, 2022: IEEE, pp. 1–2.
32. Tidy3D. " https://www.flexcompute.com/tidy3d/solver/." (accessed).
33. A. Arbabi, Y. Horie, A. J. Ball, *et al.*, "Subwavelength-thick lenses with high numerical apertures and large efficiency based on high-contrast transmitarrays," Nat. Commun. **6**(1), 7069 (2015).
34. Y. Wang, Q. Chen, W. Yang, *et al.*, "High-efficiency broadband achromatic metalens for near-IR biological imaging window," Nat. Commun. **12**(1), 5560 (2021).
35. B. Yu, J. Wen, X. Chen, *et al.*, "An achromatic metalens in the near-infrared region with an array based on a single nano-rod unit," Appl. Phys. Express **12**(9), 092003 (2019).
36. S. Shrestha, A. C. Overvig, M. Lu, *et al.*, "Broadband achromatic dielectric metalenses," Light: Sci. Appl. **7**(1), 85 (2018).
37. F. Zhao, X. Jiang, S. Li, *et al.*, "Optimization-free approach for broadband achromatic metalens of high-numerical-aperture with high-index dielectric metasurface," J. Phys. D: Appl. Phys. **52**(50), 505110 (2019).
38. H. Zhou, L. Chen, F. Shen, *et al.*, "Broadband achromatic metalens in the midinfrared range," Phys. Rev. Appl. **11**(2), 024066 (2019).